Estimating Aboveground Carbon Dynamic of China Using Optical and Microwave Remote-Sensing Datasets from 2013 to 2019

Zhongbing Chang, Lei Fan, Wigneron J.-P., Ying-Ping Wang, Philippe Ciais, Jérôme Chave, Rasmus Fensholt, Jing M. Chen, Wenping Yuan, Weimin Ju, et al.

Journal of Remote Sensing
A SCIENCE PARTNER JOURNAL

RESEARCH ARTICLE

Estimating Aboveground Carbon Dynamic of China Using Optical and Microwave Remote-Sensing Datasets from 2013 to 2019

Zhongbing Chang[1,2], Lei Fan[3*], Jean-Pierre Wigneron[4], Ying-Ping Wang[5], Philippe Ciais[6], Jérôme Chave[7], Rasmus Fensholt[8], Jing M. Chen[9,10], Wenping Yuan[11,12], Weimin Ju[13,14], Xin Li[15,16], Fei Jiang[13,14], Mousong Wu[13,14], Xiuzhi Chen[11,12], Yuanwei Qin[17], Frédéric Frappart[4,18], Xiaojun Li[4], Mengjia Wang[4,19], Xiangzhuo Liu[4], Xuli Tang[1], Sanaa Hobeichi[20], Mengxiao Yu[1], Mingguo Ma[3], Jianguang Wen[21], Qing Xiao[21], Weiyu Shi[3], Dexin Liu[22], and Junhua Yan[1*]

[1]Key Laboratory of Vegetation Restoration and Management of Degraded Ecosystems, South China Botanical Garden, Chinese Academy of Sciences, Guangzhou 510650, China. [2]University of Chinese Academy of Sciences, Beijing 100049, China. [3]Chongqing Jinfo Mountain Karst Ecosystem National Observation and Research Station, School of Geographical Sciences, Southwest University, Chongqing 400715, China. [4]INRAE, UMR1391 ISPA, Université de Bordeaux, F-33140 Villenave d'Ornon, France. [5]CSIRO Oceans and Atmosphere, Aspendale, VIC 3195, Australia. [6]Laboratoire des Sciences du Climat et de l'Environnement, CEA/CNRS/UVSQ/Université Paris Saclay, Gif-sur-Yvette, France. [7]Laboratoire Evolution et Diversité Biologique, Université Paul Sabatier, Toulouse, France. [8]Department of Geosciences and Natural Resource Management, University of Copenhagen, Copenhagen, Denmark. [9]Department of Geography and Program in Planning, University of Toronto, Toronto, ON M5S 3G3, Canada. [10]College of Geographical Science, Fujian Normal University, Fuzhou 3500007, Fujian, China. [11]School of Atmospheric Sciences, Sun Yat-sen University, Zhuhai 519082, Guangdong, China. [12]Southern Marine Science and Engineering Guangdong Laboratory, Zhuhai 519000, Guangdong, China. [13]Jiangsu Provincial Key Laboratory of Geographic Information Science and Technology, International Institute for Earth System Science, Nanjing University, Nanjing 210023, China. [14]Jiangsu Center for Collaborative Innovation in Geographical Information Resource Development and Application, Nanjing 210023, China. [15]Institute of Tibetan Plateau Research, Chinese Academy of Sciences, Beijing 100101, China. [16]CAS Center for Excellence in Tibetan Plateau Earth Sciences, Chinese Academy of Sciences, Beijing 100101, China. [17]Department of Microbiology and Plant Biology, Center for Spatial Analysis, University of Oklahoma, Norman, OK, USA. [18]LEGOS, Université de Toulouse, CNES, CNRS, IRD,UPS-14 avenue Edouard Belin, 31400 Toulouse, France. [19]State Key Laboratory of Remote Sensing Science, Faculty of Geographical Science, Beijing Normal University, Beijing 100875, China. [20]Climate Change Research Centre, University of New South Wales, Sydney, NSW 2052, Australia. [21]State Key Laboratory of Remote Sensing Science, Institute of Remote Sensing and Digital Earth, Chinese Academy of Sciences, Beijing 100101, China. [22]College of Geography and Environmental Science, Henan University, Kaifeng 475004, China.

*Address correspondence to: leifan33@swu.edu.cn (L.F.); jhyan@scib.ac.cn (J.Y.)

Citation: Chang Z, Fan L, Wigneron JP, Wang YP, Ciais P, Chave J, Fensholt R, Chen JM, Yuan W, Ju W, Li X, Jiang F, Wu M, Chen X, Qin Y, Frappart F, Li X, Wang M, Liu X, Tang X, Hobeichi S, Yu M, Ma M, Wen J, Xiao Q, Shi W, Liu D, Yan J. Estimating Aboveground Carbon Dynamic of China Using Optical and Microwave Remote-Sensing Datasets from 2013 to 2019. *J. Remote Sens.* 2023;3:Article 0005. https://doi.org/10.34133/remotesensing.0005

Submitted 22 February 2022
Accepted 20 December 2022
Published 13 January 2023

Over the past 2 to 3 decades, Chinese forests are estimated to act as a large carbon sink, yet the magnitude and spatial patterns of this sink differ considerably among studies. Using 3 microwave (L- and X-band vegetation optical depth [VOD]) and 3 optical (normalized difference vegetation index, leaf area index, and tree cover) remote-sensing vegetation products, this study compared the estimated live woody aboveground biomass carbon (AGC) dynamics over China between 2013 and 2019. Our results showed that tree cover has the highest spatial consistency with 3 published AGC maps (mean correlation value $R = 0.84$), followed by L-VOD ($R = 0.83$), which outperform the other VODs. An AGC estimation model was proposed to combine all indices to estimate the annual AGC dynamics in China during 2013 to 2019. The performance of the AGC estimation model was good (root mean square error = 0.05 Pg C and $R^2 = 0.90$

with a mean relative uncertainty of 9.8% at pixel scale [0.25°]). Results of the AGC estimation model showed that carbon uptake by the forests in China was about +0.17 Pg C year^{-1} from 2013 to 2019. At the regional level, provinces in southwest China including Guizhou (+22.35 Tg C year^{-1}), Sichuan (+14.49 Tg C year^{-1}), and Hunan (+11.42 Tg C year^{-1}) provinces had the highest carbon sink rates during 2013 to 2019. Most of the carbon-sink regions have been afforested recently, implying that afforestation and ecological engineering projects have been effective means for carbon sequestration in these regions.

Introduction

China's forested areas represent a carbon sink that contributes substantially to regional and global carbon storage [1,2]. However, both the magnitude and spatial patterns of the carbon changes in China differ across published reports. A precise quantification of the annual aboveground biomass carbon (AGC) dynamics is therefore important for understanding how China's forests contribute to the global carbon balance [3,4]. Satellite records offer the potential to monitor AGC changes by combining diverse remote-sensing sources including optical, synthetic aperture radar (SAR), light detection and ranging (LiDAR), and microwave sensors [5–10]. Yet, current assessments of the AGC dynamics in China using satellite records remain highly uncertain [11,12].

Optical vegetation indices (VIs) are related to the greenness components of the vegetation and thus indirectly to AGC [13]. VIs could provide better spatial coverage with high resolution and are available for long-term time series, which can provide effective global monitoring of vegetation trends [14]. Previous studies have used optical VIs for AGC estimation in different regions, e.g., tropical regions [5,7,15], in the USA [16,17], and in China [9,18–20]. Xu et al. [21] developed globally estimates of carbon stock changes of live woody biomass using measurements from ground, air, and space. These AGC maps were produced by integrating remote-sensing data (e.g., optical, SAR, and LiDAR) and field measurements using the machine learning methods [22,23]. They constituted the best benchmarks to date for carbon stored in living woody vegetation and have been used as benchmark maps for monitoring the AGC dynamics over the global and tropical regions [6,10,24,25]. However, optical VI signals are known to be affected by clouds and aerosols and suffer from the saturation problem in densely vegetated areas [26,27]. Moreover, the retrieved AGC values using these approaches differ in both magnitude and spatial patterns among the different studies and are available for only a single epoch, and therefore cannot be used to monitor the temporal dynamics of carbon stocks [24,28]. Although LiDAR is considered as the most promising method for estimating AGC, there was no dedicated spaceborne LiDAR designed specifically to estimate vegetation AGC until the launch of Global Ecosystem Dynamics Investigation (GEDI) in 2019 [29].

Vegetation optical depth (VOD) retrieved from microwave sensors measures the vegetation water content, thus providing a useful proxy for monitoring AGC dynamics [6,10,30–32]. Compared to optical VIs, VOD products are sensitive to both leafy and woody vegetation components and are mostly insensitive to atmospheric and cloud effects [33,34]. Changes in AGC stocks have been inferred using VOD products from multiple microwave sensors, including VOD products at high frequency (C-, X-, and K-bands, 6.9 to 18.7 GHz) [32,35–40], and at low frequency (L-band, 1.4 GHz) [41,42]. Low-frequency VOD has been shown to have better capabilities to monitor the AGC dynamics due to the higher penetration capacity of the microwave observations at large wavelengths (~20 cm at L-band) [6,10,24,25,43]. Therefore, L-band VOD (L-VOD) is less sensitive to saturation effects and more sensitive to AGC held in stems and branches than high-frequency VOD products [44,45]. Yet, radio frequency interference (RFI) at L-band degrades locally the performance of L-VOD for monitoring of AGC [46,47], especially over some regions in China. High-frequency VOD products are less affected by RFI but can suffer from saturation in dense forests [48].

Given the respective weaknesses and advantages of VODs and VIs, combining the 2 types of data could be a potential way to improve the quantification of the AGC dynamics [45,49–51]. Assessing the sensitivity of VODs and VIs to AGC is, however, an essential preliminary step in any attempt to monitor AGC dynamics from remote-sensing. The performance of VODs for AGC monitoring has been evaluated at global [48,52,53] or regional scales, for example, in tropical regions [54–56], Australia [57,58], and the USA [59]. However, there is a lack of studies in China, especially considering the strong influence of RFI on L-VOD over China [47].

Several empirical functions have been proposed to spatially regress AGC against VOD at large scales, e.g., linear regressions [24], arctangent regressions [6,32,43], and logistic regressions [48,55]. However, the relationships between AGC and VODs/VIs are quite complex and may not be well captured by these regression functions [48,54]. As an effective tool to fit complex data with nonlinear partial relations, machine learning approaches have been increasingly used for forest structure and AGC mapping [21,60]. Among all machine learning approaches, random forest (RF) models [61] show excellent performance in modeling the complex relationships between different land surface variables and AGC [62]. An advantage of RF is that multiple predictors can be incorporated without making further assumptions about their covariance structure, which makes RF models suitable for describing nonlinear relationships between AGC and VODs/VIs.

The objectives of this study are as follows: (a) to assess the performances of 3 VODs (e.g., L-VOD, IB-VOD, and LPDR-VOD) and 3 optical VIs (e.g., normalized difference vegetation index [NDVI], leaf area index [LAI], and tree cover [TC]) in predicting AGC across China using 3 AGC benchmark maps; (b) to produce AGC products from the combination of VODs and VIs using a RF model; and (c) to quantify the interannual dynamics of AGC stocks across China for the period 2013 to 2019.

Materials

Forests, which cover more than 20% of mainland China [3], are mainly located in the northeastern, southern, and southwestern regions. Over the past 2 decades, ecological restoration projects were implemented in several regions (Fig. 1), including: Three-North Shelter Forest Program, Tibetan Plateau, Loess Plateau, and Southern China [63].

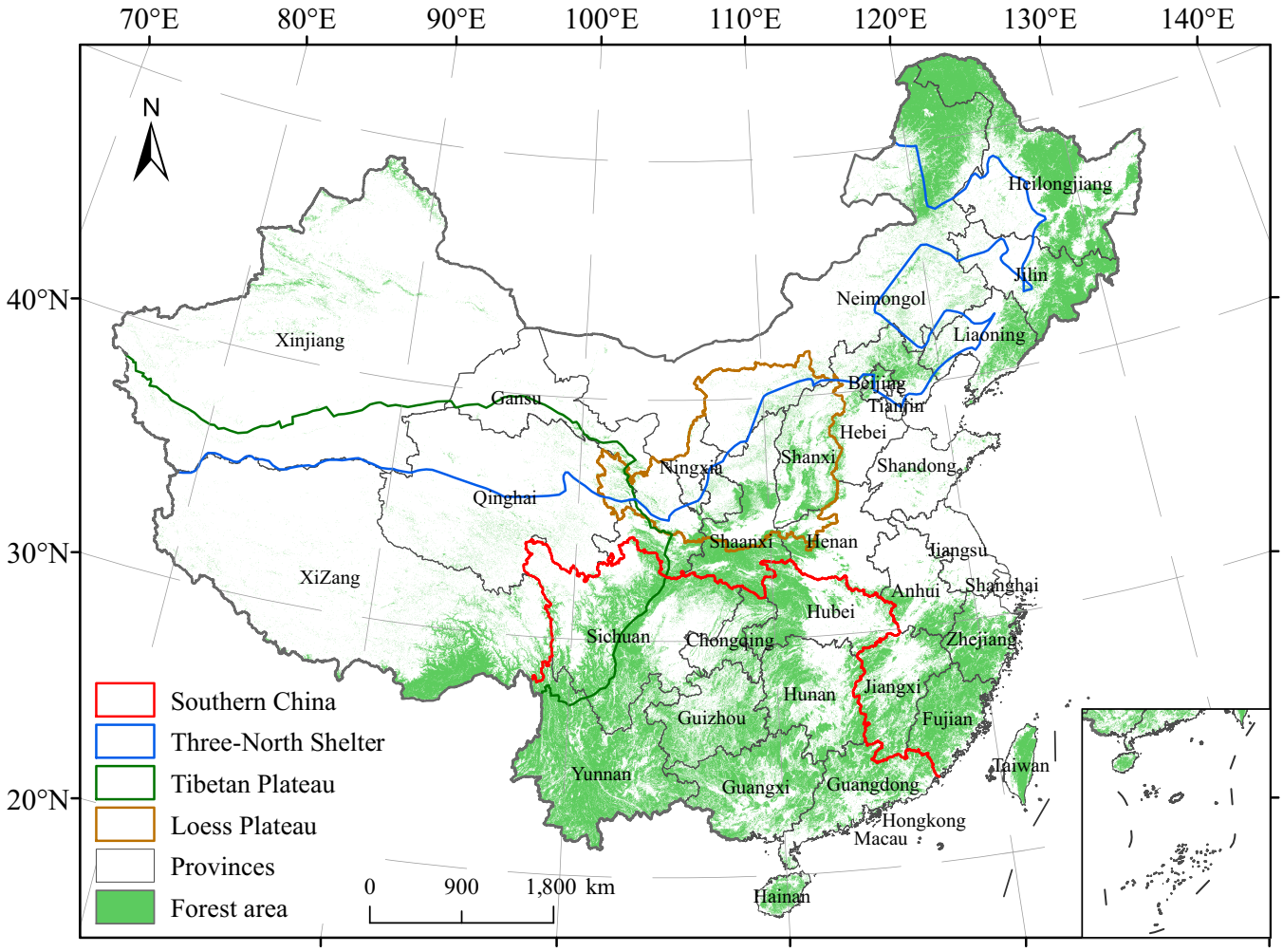

Fig. 1. Location of the provinces and 4 main ecological restoration regions (the Three-North Shelter, Tibetan Plateau, Loess Plateau, and Southern China) in China.

Microwave VOD products

L-VOD

L-VOD was retrieved from the Soil Moisture and Ocean Salinity (SMOS) satellite using the SMOS-IC algorithm (version 2) [41,42]. Version 2 of the L-VOD product provides daily global L-VOD and soil moisture (SM) retrieved from the ascending and descending data at 0.25° resolution for 2010 to 2020. The L-VOD product was retrieved by the L-band (1.4 GHz) microwave emission of the biosphere model, without any auxiliary hydrology or vegetation products as inputs [64]. In this study, the observations affected by RFI for which root mean square error (RMSE) associated with the L-VOD product is larger than 8 K were filtered out. In addition, observations affected by strong topography, frozen conditions, and the sum of urban, water and ice fractions higher than 10% were excluded [41]. The yearly L-VOD values for a given pixel were calculated as the medians of all available ascending and descending retrievals in the year. The SMOS-IC L-VOD product was selected here as it has been shown to exhibit a stronger relationship with AGC than other SMOS products [55].

IB-VOD

The IB-VOD product was retrieved by the X-band microwave emission of the biosphere model [39]. IB-VOD was retrieved from the Advanced Microwave Scanning Radiometer 2 (AMSR2) X-band (10.7 GHz, with a spatial resolution of 0.25°) descending data (local time = 1:30 AM) considering proximal conditions of the air, canopy, and soil at night. To avoid the ill-posed issue caused by retrieving both SM and VOD from mono-angular and dual-polarized observations (AMSR2), the X-band microwave emission of the biosphere model uses the ERA5 SM product [65] as input.

LPDR-VOD

LPDR-VOD was derived from the land parameter data record (LPDR, version 2) [35]. LPDR provides a long-term (2002 to 2020) global record of the daily X-VOD products at 0.25° resolution. It is retrieved from the AMSR for Earth Observing System (AMSR-E) and AMSR2 sensors at 10.7 GHz based on both ascending (13.30) and descending (01.30) data. Grid cells affected by frost conditions, large water bodies, strong precipitation, or RFI were excluded using the quality assessment files [66].

Optical VIs

We applied 3 optical VIs in this study that are commonly used to estimate AGC in previous studies (Table 1) [22,67], including:

1. NDVI, provided by the monthly MODIS product (MOD13A3) at 1-km spatial resolution [68]. NDVI is

Table 1. Overview of the VODs, VIs, and benchmark AGC datasets used in this study.

Dataset	Products/Sensor	Period	Resolution	Temporal	Reference
L-VOD	SMOS-IC V2	2013–2019	0.25°	Daily	Fan et al. [6]
IB-VOD	AMSR2	2013–2019	0.25°	Daily	Wang et al. [12]
LPDR-VOD	AMSE-E and AMSE2	2013–2019	0.25°	Daily	Du et al. [35]
NDVI	MOD13A3	2013–2019	1 km	Monthly	Didan. [68]
LAI	MOD15A2	2013–2019	500 m	8 d	Myneni et al. [71]
TC	MOD44B	2013–2019	250 m	Yearly	Dimiceli et al. [73]
Saatchi	GLAS LiDAR, QSCAT radar, field data, NDVI, LAI, and SRTM	2015	1 km	Yearly	Saatchi et al. [7]
CCI	Sentinel-1, ALOS-2 PALSAR-2, field data, canopy height, and SRTM	2017	100 m	Yearly	Santoro and Cartus. [76]
Saatchi-WT	Data fusion	2010s	1 km	Yearly	Supplementary Text

widely used to monitor vegetation cover [69,70] and biomass [13,16].

2. LAI, derived from the 8-day MODIS product (MOD15A2) at 500-m spatial resolution [71]. LAI is an important indicator of plant growth and radiation use efficiency [72].
3. TC, derived from the yearly MODIS product (MOD44B) at 250-m spatial resolution [73], represents the percent tree canopy (≥5 m) cover [74].

In this study, the pixels with snow or cloud were filtered out using the quality assessment data accompanying the product. Usually, only NDVI and EVI are referred to as vegetation indices. But for convenience, NDVI, EVI, LAI and TC products were referred to as vegetation indices as in previous studies [52]. All VI products were aggregated to 0.25° through simple averaging to match the spatial resolution of VODs.

AGC benchmark maps

This study used 3 AGC benchmark maps to assess the performances of VIs and VODs to AGC (Table 1), including:

1. Saatchi map, estimating AGC in the pan-tropics at 1-km resolution by merging data from field measurements, GLAS LiDAR, MODIS, and Quick Scatterometer [7]. The Saatchi map used here is an updated version that represents global AGC for 2015 by combining data from the SRTM, Landsat, and Advanced Land Observing Satellite (ALOS) [75].
2. Climate Change Initiative (CCI) map, a global map of AGC at 100-m resolution for 2017 using multiple remote-sensing observations [76]. The CCI map was produced by combining data from the SAR C-band Sentinel-1 and L-band ALOS-2 Phased Array L-band SAR (PALSAR-2).
3. Saatchi-WT map, produced by merging the forest AGC map and nonforest AGC map [77]. The forest and nonforest regions were identified using the Liu et al. [78] land cover map [78]. The forest AGC map was estimated using a weighting technique (WT) method to merge the 5 published AGC products [5,7–9,19]. The WT method was trained using independent field observations across China [79] (Supplementary Text). The nonforest AGC map was computed from the Saatchi map over nonforest regions.

The spatial resolution of all AGC maps was aggregated to 0.25° by simple averaging. The units of biomass density (Mg/ha) were converted to carbon density (Mg C/ha) by multiplying the original values by 0.5 [5].

Methods

In this study, we focused on aboveground carbon stocks for live woody vegetation and masked the nonvegetated pixels dominated by the following land-cover classes: "settlement", "water", "bare and sparse vegetation", and "wetland" using the CCI land cover dataset [80].

Considering the availability of the products, only L-VOD, LPDR-VOD, NDVI, LAI, and TC were used for estimating AGC. The VODs and VIs in the same year 2015 were chosen as the baseline for model calibration. We then estimated the yearly AGC dynamics across China for the period 2013 to 2019.

Comparison of VIs and VODs to benchmark AGC maps

The relationship of VIs and VODs to AGC was indicated by the Pearson correlation coefficient R [81] (Eq. 1) by comparing the AGC datasets with VIs and VODs, as defined below:

$$R = \frac{\sum \left(VOD - \overline{VOD}\right)\left(AGC - \overline{AGC}\right)}{\sqrt{\sum \left(VOD - \overline{VOD}\right)^2 \sum \left(AGC - \overline{AGC}\right)^2}} \quad (1)$$

where VOD and AGC are the values of VOD and benchmark AGC, respectively. $\overline{VOD}$ and $\overline{AGC}$ are the average values of VOD and benchmark AGC, respectively. We used P value ($P < 0.05$) to define the significance level of the correlation.

Estimation of AGC using RF

The yearly AGC stocks were estimated by combining VODs and VIs with RF models [61]. Firstly, an AGC model hereafter AGC_{main} given by Eq. 2 was trained using all 5 predictors in 2015

(L-VOD (VOD_L), LPDR-VOD (VOD_{LPDR}), NDVI, LAI, and TC), and the benchmark AGC maps were the response variables. The AGC_{main} model was expressed as the linking model (f) between benchmark AGC and the predictors in the framework of RF:

$$AGC_{main} = f\left(VOD_L, VOD_{LPDR}, NDVI, LAI, TC\right) \quad (2)$$

where AGC_{main} is the retrieved AGC value.

As there were missing values in the AGC_{main} estimates caused by the missing observations of L-VOD affected by RFI [41,47], an alternative AGC model (AGC_{noLVOD}, Eq. 3), as a supplementary model to AGC_{main}, was trained using the same predictors but without L-VOD. The supplementary AGC model (hereafter AGC_{noLVOD}) was defined as:

$$AGC_{noLVOD} = f\left(VOD_{LPDR}, NDVI, LAI, TC\right) \quad (3)$$

AGC_{noLVOD} was used to predict AGC estimates for pixels with missing estimates from AGC_{main}. In a final step a model (AGC_{merge}, Eq. 4) was defined to merge AGC_{main} and AGC_{noLVOD} to estimate the annual AGC density from 2013 to 2019.

$$AGC_{merge} = merging\left(AGC_{main}, AGC_{noLVOD}\right) \quad (4)$$

The AGC_{merge} model was then applied to the data for each year to derive maps of annual AGC density for 2013 to 2019.

To account for the uncertainties in the benchmark AGC maps, we used all 3 AGC maps to train the AGC model. Thus, 3 calibrated AGC models were obtained. Following Fan et al. [6], assuming that a good calibration result could be obtained, the AGC model adds a temporal dimension to static maps and provides a "space for time" replacement. The mean of these 3 AGC values was calculated to estimate the yearly AGC maps during 2013 to 2019 across China. The range (i.e., minima and maxima) of the 3 AGC values were also calculated, as they provide the uncertainty for the retrieved AGC estimates.

Validation of AGC estimates

We used a bootstrap and cross-validation method to evaluate the performance of AGC_{main}, AGC_{noLVOD}, and AGC_{merge}. Three sets of bootstrapped AGC estimates were computed on the basis of 3 calibrations of the AGC model. A bootstrap sampling method (sampling rate = 80%, iterations = 1000) was used to calibrate each AGC model (e.g., AGC_{main}, AGC_{noLVOD}, and AGC_{merge}); the remaining (20%) was used for the validation of the AGC estimates. The uncertainties associated with the AGC estimates were evaluated using 2 metrics, including the adjusted coefficient of determination (R^2) and RMSE between the benchmark AGC maps and the RF-derived AGC estimates. Also, the trends and the changes of AGC_{main} were compared with AGC_{noLVOD} for their overlap pixels, to confirm that AGC_{noLVOD} provide similar results to AGC_{main}.

The uncertainties in the AGC_{merge} estimates at pixel scale ($Uncertainties_{pixel}$(%)) were defined as the RMSE of the AGC_{merge} model ($RMSE_{AGC_{merge}}$) relative to the AGC density from the corresponding benchmark maps ($AGC \cdot density_{benchmark \cdot map}$), expressed as Eq. 5. $RMSE_{AGC_{merge}}$ at the pixel scale was estimated using the bootstrap approach mentioned above.

$$Uncertainties_{pixel}(\%) = \frac{RMSE_{AGC_{merge}}}{AGC \cdot density_{benchmark \cdot map}} \quad (5)$$

Results

Comparison of VIs and VODs to the AGC benchmark maps

All VOD products showed similar spatial patterns with VIs and benchmark AGC maps (Fig. 2A to C): high VODs/VIs/AGC values can be observed in the forests of southern and northeastern China, and low VODs/VIs/AGC values can be observed in the temperate steppe and Qinghai-Tibet plateau alpine. However, large differences can be observed among the 3 benchmark AGC estimates (Fig. 2G to I). In consideration of the total carbon stock in the 3 benchmark AGC maps (Table S1), the values range from 10.23 Pg C (CCI), 12.57 Pg C (Saatchi-WT), to 14.61 Pg C (Saatchi). These differences in AGC stocks can be partly explained by the fact that these benchmark maps have different coverage, which were limited by the different AGC retrieval methods [67]. Another potential reason is that all AGC benchmark maps contain uncertainties and biases [18]. Thus, we used all the different maps to construct the RF model estimating the AGC dynamics over China in this study.

Before carrying out the retrievals of AGC, we firstly compared the VIs/VODs indices against the 3 benchmark AGC maps and found nonlinear relationships (Fig. 3 and Figs. S1 to S2). The highest correlation between the VIs and the benchmark AGC products was obtained for the TC product (R = 0.80 to 0.88), followed by NDVI (R = 0.65 to 0.75), while the lowest correlations were found for LAI (R = 0.60 to 0.68) (Table 2). As an example, it can be seen that NDVI and LAI quickly saturate for Saatchi AGC values above 25 Mg C/ha (Fig. 3D and E). Similar results can be found for the comparison between VIs and other benchmark maps, e.g., CCI (Fig. S1) and Saatchi-WT maps (Fig. S2).

With respect to VODs, L-VOD showed the highest correlation with benchmark AGC maps (R = 0.80 to 0.85), followed by LPDR-VOD (R = 0.72 to 0.80) and IB-VOD (R = 0.67 to 0.74) (Table 2). As an example, the scatterplots between L-VOD and Saatchi AGC showed noticeable variation when AGC > 75 Mg C/ha (Fig. 3A). For IB-VOD and LPDR-VOD, both of them tended to saturate with AGC values greater than 50 Mg C/ha (Fig. 3B and C). Similar results can be seen for the comparison of VODs against the CCI (Fig. S1) and Saatchi-WT (Fig. S2) maps. In summary, IB-VOD and LPDR-VOD all display saturated signals when AGC values are greater than 50 Mg C/ha, whereas L-VOD shows a higher spatial correlation to AGC without strong signs of saturation.

The intercomparisons between VIs/VODs and benchmark AGCs were made to evaluate their expected performance for monitoring AGC, using the mean values of R as an indicator (Table 2). In summary, we found the highest correlation values were obtained by TC (with a mean value of R of 0.84), followed by L-VOD (R = 0.83), LPDR-VOD (R = 0.76), IB-VOD (R = 0.71), NDVI (R = 0.70), and LAI (R = 0.65).

Calibration and evaluation of the AGC estimation models

The AGC_{main} model was produced by merging optical and microwave indices with a RF algorithm. However, the missing estimates of the AGC_{main} model are found over southern and eastern China, limited by the availability of L-VOD data (Fig. 4A). As a supplement model, AGC_{noLVOD} was used to provide AGC estimates for pixels with missing estimates from the AGC_{main} model. The AGC_{noLVOD} estimates almost covered the whole study region;

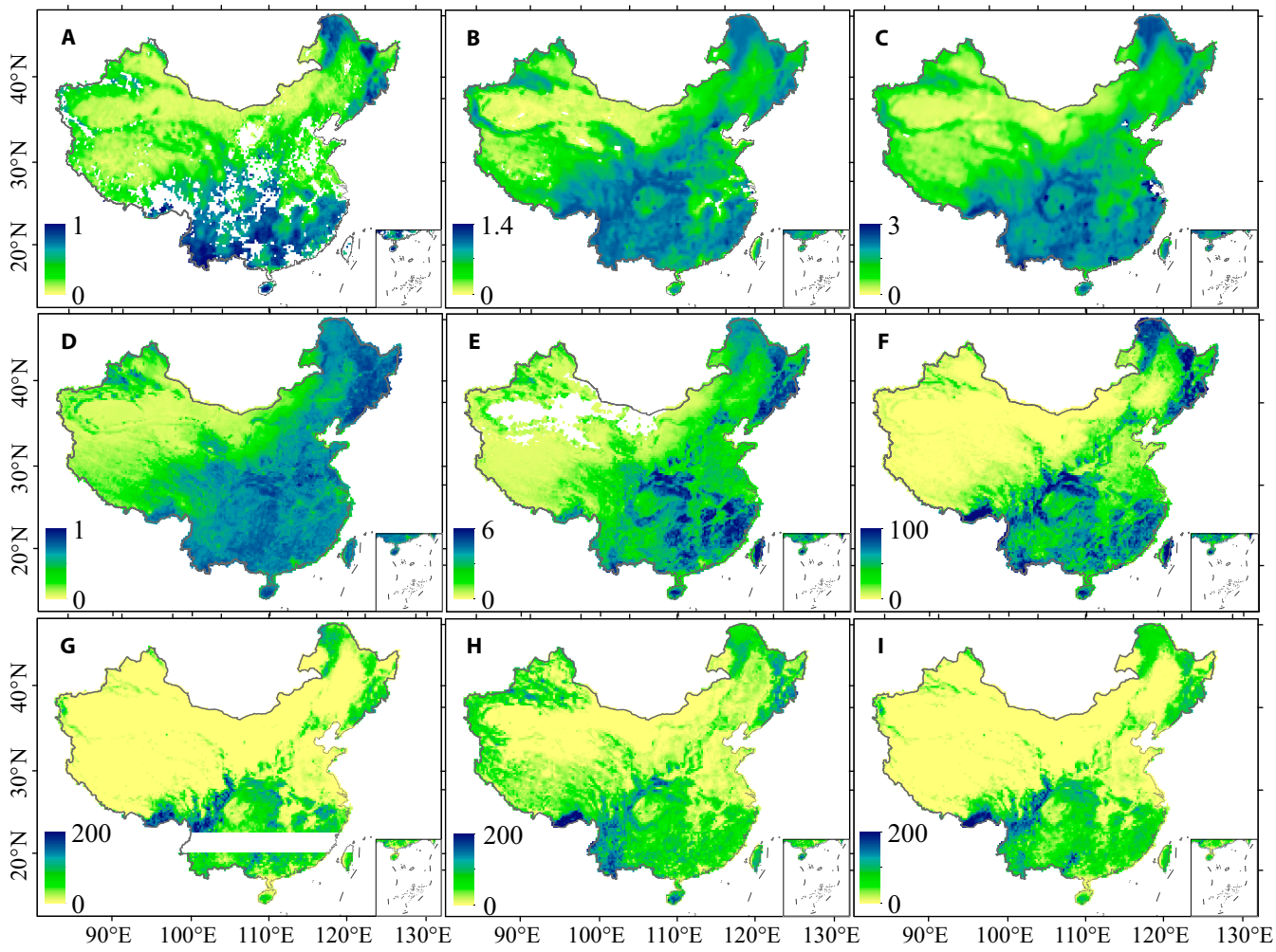

Fig. 2. Yearly VODs, VIs, and benchmark AGC maps. (A) L-VOD for 2015, (B) IB-VOD for 2015, (C) LPDR-VOD for 2015, (D) NDVI for 2015, (E) LAI for 2015, (F) TC for 2015, and benchmark AGC of (G) Saatchi, (H) CCI, and (I) Saatchi-WT.

thus, combining AGC_{main} and AGC_{noLVOD} provided a higher spatial coverage (81%) of China, relative to that obtained from the AGC_{main} estimates (63%) (Fig. 4B and C). The percentage increase of mean-squared error (%IncMSE) was calculated to evaluate the importance of each variable in RF model. As can be seen from Fig. S4, TC and L-VOD products were found the most important predictors in the RF model.

Both the AGC_{main} and AGC_{noLVOD} models nicely fit the spatial pattern of benchmark AGC, as indicated by the high R^2 (0.90, 0.89 for AGC_{main} and AGC_{noLVOD} models) and low RMSE values (8.6 Mg C/ha and 9.3 Mg C/ha for AGC_{main} and AGC_{noLVOD} models) (Fig. 5). Taking the Saatchi map as an example, both AGC_{main} and AGC_{noLVOD} have overcome the saturations issues observed in relationships derived from single index: AGC_{main} and AGC_{noLVOD} can fit the spatial changes for AGC stocks larger than 100 Mg C/ha. A similar ability of AGC_{main} and AGC_{noLVOD} can be observed for low carbon density, while single index generally showed a high dispersion (e.g., L-VOD, Fig. 3A).

In the regions of overlap between the AGC_{main} and AGC_{noLVOD} estimates, the general trends and the magnitude of the changes in AGC_{main} are very similar to those in AGC_{noLVOD} (Fig. 6). For example, both the AGC_{main} and AGC_{noLVOD} estimates calibrated with the Saatchi map (Fig. 6A) showed generally a net increase in AGC stocks during 2013 to 2017 and an AGC decrease in 2017, in line with the AGC dynamics from the estimates calibrated by the other benchmark maps (Fig.6B and C).

In terms of magnitude of AGC changes, the net AGC changes estimated from AGC_{noLVOD} are 12% to 16% higher than those estimated from AGC_{main} over the study period (Fig. 6). As the AGC_{noLVOD} model was only used over 26% of the study region, this difference will contribute to only a difference of 3% to 5% of the net AGC changes over China during 2013 to 2019. This suggests that the slight differences in the AGC estimates from the AGC_{noLVOD} and AGC_{main} models can be neglected when we consider the whole study period/area. In the following, we will focus on AGC estimates obtained from the model (AGC_{merge}) merging the AGC_{noLVOD} and AGC_{main} models. The general trends and the magnitude of the AGC_{merge} dynamics using 3 sets of calibrated parameters are very similar for the 3 estimates (Fig. 7). The general trends of the changes from each variable are very similar to those from AGC (Fig. S5).

Furthermore, the cross-validation using a bootstrap method showed that the AGC stocks estimated by AGC_{merge} combining AGC_{main} and AGC_{noLVOD} have a high accuracy, as indicated by a RMSE of 0.05 Pg C. The good performance of AGC_{merge} is also indicated by the high R^2 of 0.90 and low relative uncertainties (9.8%) in the pixel-scale AGC density estimates. Moreover, a better performance of AGC_{merge} can be observed at AGC density

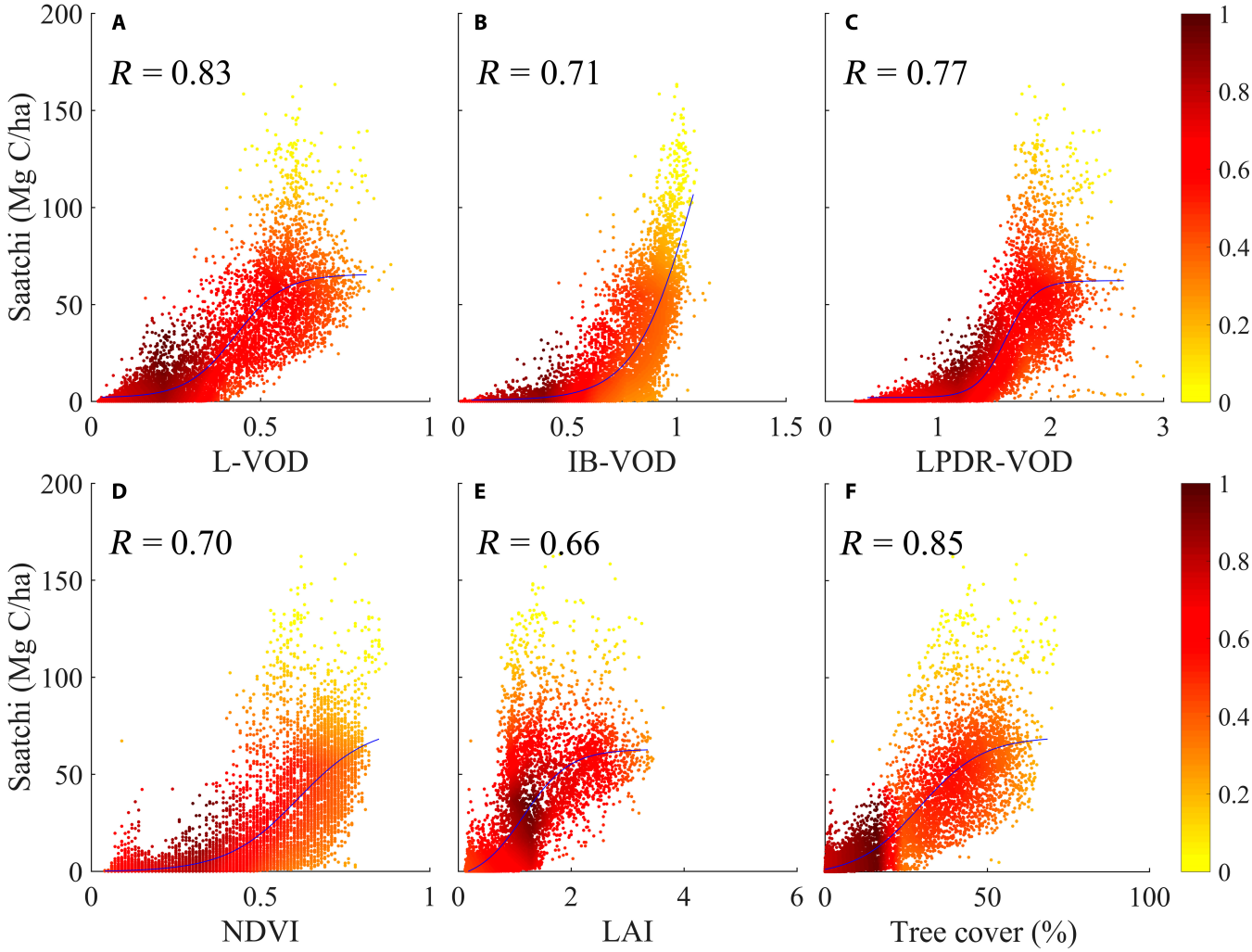

Fig. 3. The spatial relationship (*R*) between Saatchi AGC and VIs/VODs from (A) L-VOD, (B) IB-VOD, (C) LPDR-VOD, (D) NDVI, (E) LAI, and (F) TC. Solid blue lines are the fits by a logistic function following Rodríguez-Fernández et al. [55] with the parameters given in Table S1.

larger than 40 Mg C/ha (with relative uncertainties lower than 10%), relative to low AGC density (lower than 40 Mg C/ha) where the relative uncertainties are larger than 10% (Fig. 8B). The latter mainly correspond to the areas distributed across northern China (Fig. 8A). These results showed that the AGC_{merge} model has a satisfactory accuracy for estimating AGC stocks over China.

AGC dynamics over the study period

The yearly AGC across China estimated by the AGC_{merge} model showed a net AGC sink of +0.17 Pg C year^{-1} during 2013 to 2019 (the value is a mean estimated from 3 calibrations; a positive value indicates a net sink of carbon in aboveground biomes; Fig. 9A). Rapid AGC increases can be observed in 2014 to 2016 (+0.26 Pg C year^{-1}) and 2018 to 2019 (+0.15 Pg C year^{-1}),

Table 2. Spatial correlation (*R*) between VIs/VODs and benchmark AGCs using Eq. 1.

Products	L-VOD	IB-VOD	LPDR-VOD	NDVI	LAI	TC	Mean
Saatchi	0.83	0.71	0.77	0.70	0.66	0.85	0.75
CCI	0.80	0.67	0.72	0.65	0.60	0.80	0.71
Saatchi-WT	0.85	0.74	0.80	0.75	0.68	0.88	0.78
Mean	0.83	0.71	0.76	0.70	0.65	0.84	--

Note: All the correlations are significant considering the criteria $P < 0.05$.

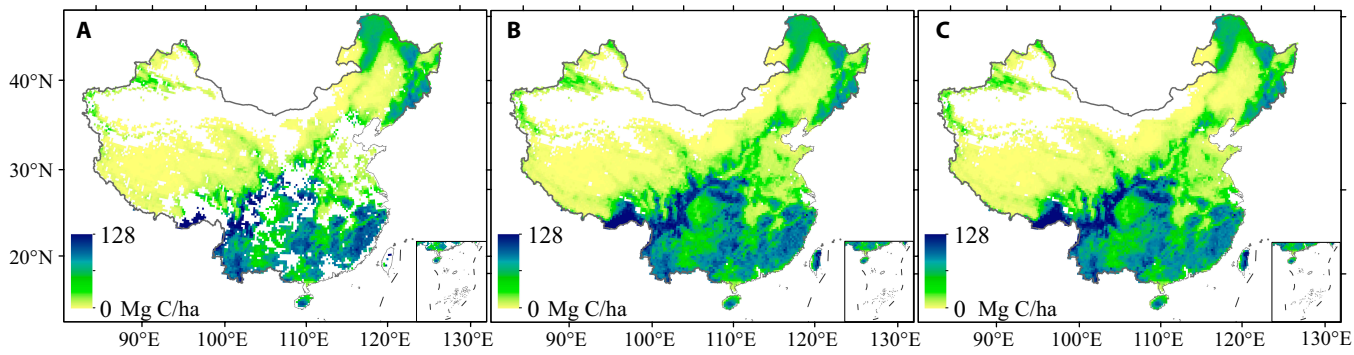

Fig. 4. The AGC estimates from (A) AGC_{main}, (B) AGC_{noLVOD}, and (C) AGC_{merge} models in 2015. The AGC estimates were computed as the median AGC values obtained from the 3 calibrated AGC models.

albeit with AGC losses of −0.14 Pg C in 2017. Carbon losses (−0.02 Pg C year^{-1}) from areas between 40°N to 50°N of China (Northeast China) were offset by a carbon sink (+0.19 Pg C year^{-1}) in the rest of the regions. The largest carbon sink (+0.10 Pg C year^{-1}) was found around 20°N to 35°N of southern China (Fig. 10), which accounts for 56% of the total carbon sink in China. The carbon sink of southern China is mainly attributed to the Guizhou (+22.35 Tg C year^{-1}) and Sichuan (+14.49 Tg C year^{-1}), followed by the Hunan (+11.42 Tg C year^{-1}), Yunnan (+8.11 Tg C year^{-1}), Guangdong (+7.37 Tg C year^{-1}), and Guangxi (+5.22 Tg C year^{-1}) provinces. Guizhou is also the province having the largest carbon sink over China in the study period. The carbon sink of the Qinghai and Tibet provinces, as referred to as the "Tibetan Plateau", ranked 4th (+9.79 Tg C year^{-1}) and 5th (+9.33 Tg C year^{-1}) among all provinces. Other regions supported by ecological restoration projects also showed a carbon uptake (Figs. 9 and 10): Loess Plateau (including the Shaanxi, Ningxia, and Shanxi provinces) has a net carbon sink of +0.03 Pg C year^{-1}, and North Shelter Forest (e.g., Xinjiang, Gansu, and Neimongol provinces) has a carbon increase of +0.01 Pg C year^{-1}. It is worth noting that Northeast China (e.g., Heilongjiang, Jilin, and Liaoning provinces) showed a carbon losses of −0.02 Pg C year^{-1} during 2013 to 2019.

Discussion

Intercomparison between VIs/VODs and benchmark AGC maps

The highest correlation between VIs and AGC benchmark maps were found for the MODIS TC products (Fig. 3). The possible reasons could be that the TC product is not fully independent from the benchmark AGCs, given that the VIs such as NDVI and TC were used as inputs for the retrieval of benchmark AGCs [5,7,9], and these VIs are all derived from MODIS reflectance bands. Moreover, previous independent evaluations found errors in the MODIS TC product, such as overestimation in sparsely vegetated areas and underestimation in densely vegetated areas

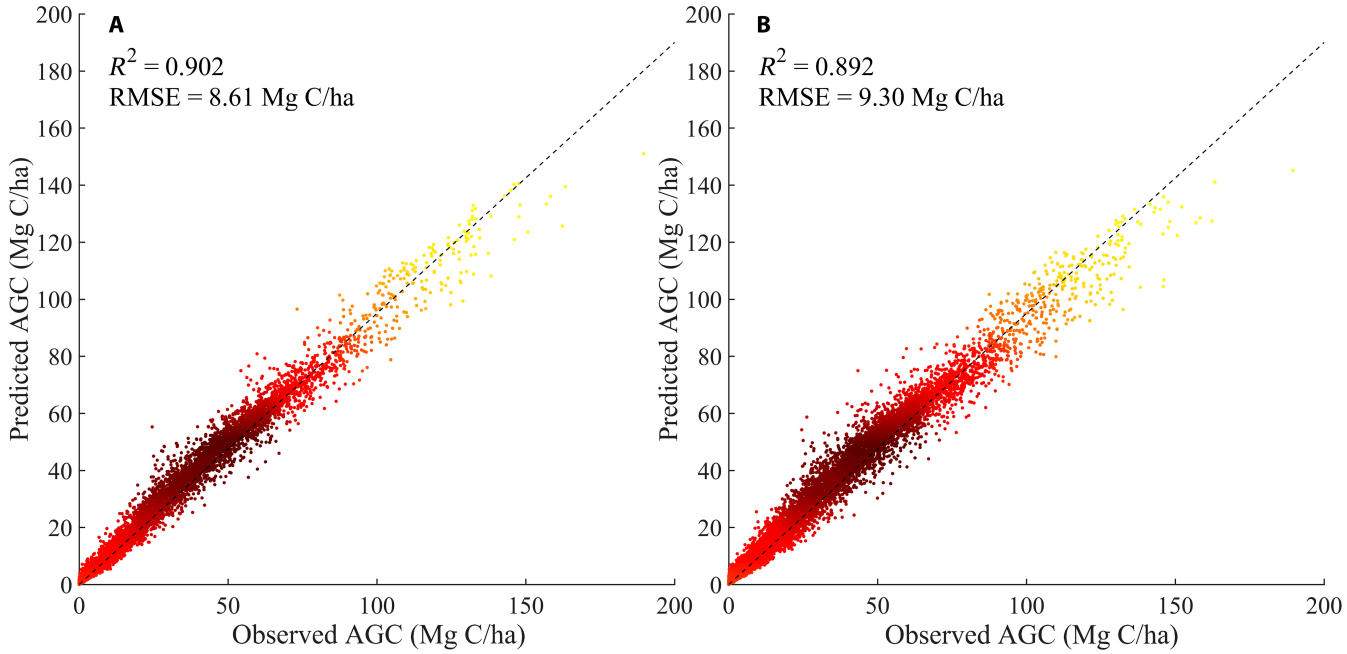

Fig. 5. Performance of the 2 RF models using different predictors based on the Saatchi map, calculated using a bootstrap cross-validation method (sampling rate = 80%, iterations = 1000). (A) AGC_{main} using VOD_L, VOD_{LPDR}, NDVI, LAI, and TC. (B) AGC_{noLVOD} using VOD_{LPDR}, NDVI, LAI, and TC. The colors show the density of scatter plots.

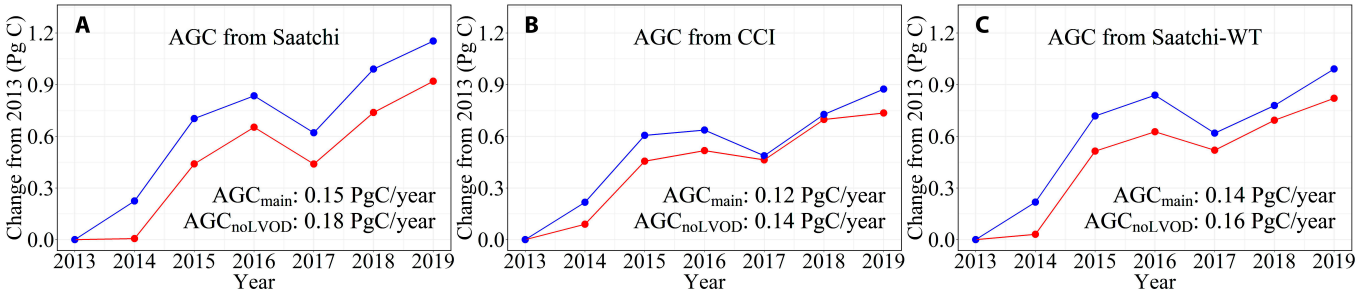

Fig. 6. Comparisons between AGC_{main} and AGC_{noLVOD} changes over the areas of overlap. The AGC changes were expressed by the AGC stocks relatively to 2013. AGC changes estimated by the benchmark AGC maps of (A) Saatchi, (B) CCI, and (C) Saatchi-WT.

[82,83]. Compared to ground reference data, previous studies showed that the MODIS TC product was affected by overestimations in croplands in regions such as South America and Southeast Asia [84] and was affected by severe underestimations in semiarid drylands [85].

Our results indicated that optical VIs such as NDVI and LAI have low correlations with benchmark AGCs and are saturated over dense vegetation with AGC values higher than 25 Mg C/ha (Figs. S1 and S2), in agreement with previous studies [52,55]. To compare the relationship linking VOD and AGC to the relationship between other VIs and AGC, scatter plots similar to those of Fig. 3 were computed using Saatchi's AGC with respect to NDVI and EVI (Fig. S3). It can be seen that there are no noticeable differences between NDVI and EVI, and both NDVI and EVI quickly saturate for AGC values above 50 Mg C/ha. These results are likely to be related to the fact that NDVI, EVI, and LAI are sensitive to the green vegetation cover, and not to the total AGC in dense vegetation [70]. However, VIs could provide better spatial coverage with high resolution and are available for long-term time series, which can provide effective global monitoring of vegetation trends [14]. A complementary use of VIs and VODs can thus allow for more complete monitoring of vegetation resources [51].

Among VODs, the spatial correlation between L-VOD and benchmark AGCs is higher than for the other VODs (Fig. 3A to C). This is due to the stronger penetration capacity of VOD retrieved at the L-band than at the C- and X-bands [46] and is thus more sensitive to the vegetation features of the whole canopy, including also the woody component [47,86]. This agrees with Li et al. [48] that showed that L-VOD maps are better correlated with AGC benchmark maps than higher-frequency VOD products (e.g., X-VOD and C-VOD) at the global scale.

Note that both IB-VOD and LPDR-VOD tended to saturate for AGC values higher than 50 Mg C/ha (Figs. S1 and S2). This result supports the findings of Chaparro et al. [54], who found that VOD at higher frequencies (e.g., X-band and C-band), as well as optical indices, saturates in dense vegetation in the tropics. This may lead to uncertainties in the AGC estimation using IB-VOD and LPDR-VOD in the tropical forests of southern China. Conversely, IB-VOD and LPDR-VOD products are more sensitive to the top of the canopy vegetation features, making them more suitable for monitoring temporal changes in the green vegetation components [46,48].

Regarding the different benchmark AGC maps, the best correlation values of benchmark AGCs with VIs and VODs were generally observed for the Saatchi-WT map (with a mean value of $R = 0.78$), followed by the Saatchi map (with a mean value of $R = 0.75$) (Table 2). This is in line with the findings of Chang et al. [77] showing that the Saatchi-WT map showed better accuracy than the other AGC products, when comparing them against in situ measurements. However, it is worth noting that all benchmark maps used information from MODIS VIs, due to the limited availability of independent sources of LiDAR, although GEDI can provide more observations for biomass in the following years [29]. The high correlation between the independent VODs and AGCs provide an alternative way to estimate AGC stocks, as proposed in this study.

Continuous carbon sink over China

Our estimated carbon sink (+0.17 Pg C year^{-1}) during 2013 to 2019 are comparable to the values (+0.17 Pg C year^{-1}) obtained during the 2000s reported by Jiang et al. [11] (Table 3). Also, the recent estimates by Harris et al. [87] indicated that forests in China were a net carbon sink of +0.14 Pg C year^{-1} during 2000 to 2019, which is close to our estimates for woody vegetation. Our estimates are comparable to recent estimates from Xu et al. [21] using multiple remote-sensing dataset, who reported a net carbon gain in live biomass of China of +0.17 Pg C year^{-1} for

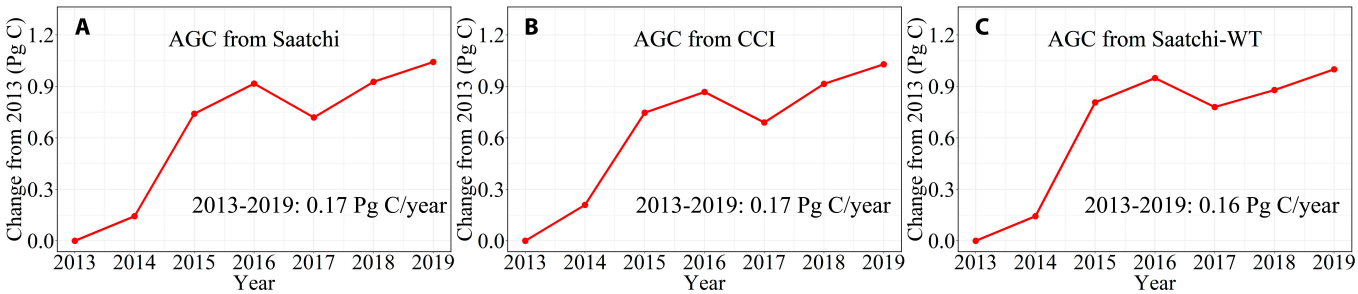

Fig. 7. AGC changes over China relatively to 2013 estimated by AGC_{merge} calibrated by different benchmark AGC maps. AGC changes estimated by the benchmark AGC maps of (A) Saatchi, (B) CCI, and (C) Saatchi-WT.

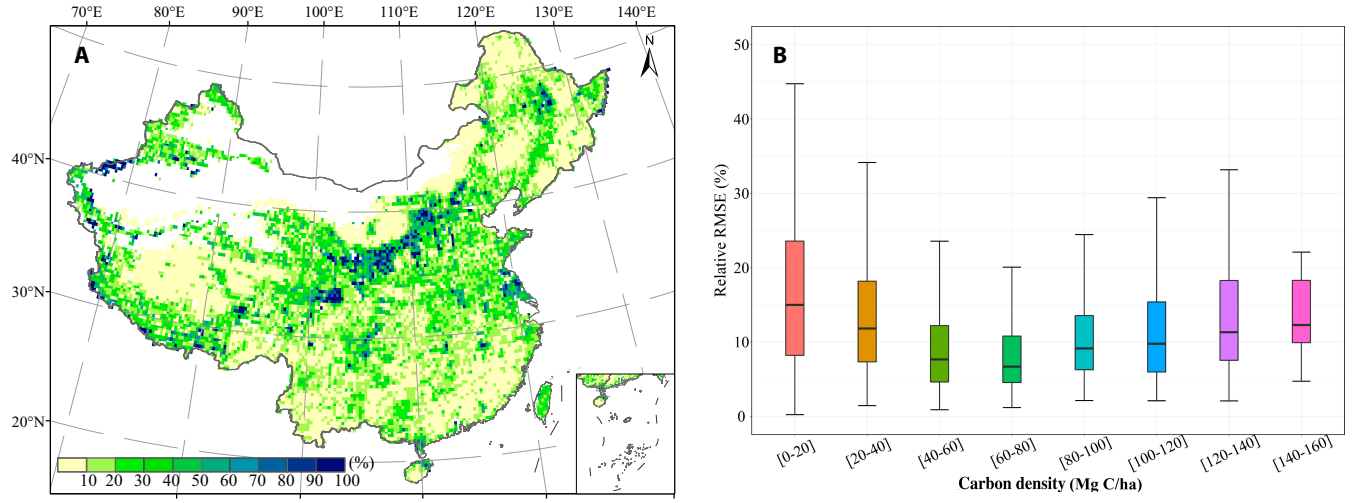

Fig. 8. Maps of the uncertainties of AGC_{merge} ($Uncertainties_{pixel}$) in 2015 in terms of spatial patterns (A) and $Uncertainties_{pixel}$ associated with AGC density (B).

2013 to 2019. These results confirmed that China has been a carbon sink in regards to biomass over the past 2 decades.

At the regional scale, in southern China, we found an increase of AGC of +0.10 Pg C year^{-1}, which is quite similar to the estimate of +0.11 Pg C year^{-1} obtained by Tong et al. [25] for 2002 to 2017 (Figs. 9 and 11). This also supports the results of Brandt et al. [88] and Tong et al. [89], which have found increased vegetation growth and carbon stocks in southern China during the recent decade. In southern China, our results suggested that the regions with the largest carbon sinks are the Guizhou, Hunan, and Guangdong provinces, in line with the findings of Wang et al. [12]. This can be explained primarily by increasing areas of newly planted forests, as a consequence of intensive national afforestation/reforestation programs implemented in the past few decades [63,90].

In northeast China, our results indicated a carbon loss of −0.02 Pg C year^{-1}. In that region, Piao et al. [2] estimated a small carbon source (−0.004 Pg C year^{-1}) during the 1980s and 1990s using both inventory-satellite-based and atmospheric inversion methods. This carbon loss was probably caused by overharvesting and degradation of forests [2,78].

Our estimates of the carbon sink are lower than the estimates using inversion of atmospheric data. For example, the inversion results constrained by ground-based and space-based measurements of atmospheric CO_2 indicated a net terrestrial CO_2 sink in China of about 0.30 to 0.43 Pg C year^{-1} in 2010 to 2015 [91–93]. Relative to our results, this larger carbon sink values could be explained by the fact that our estimates do not account for the contribution for carbon sink from belowground vegetation biomass and soil organic matter.

Relative to the results for the 1980s and 1990s, the magnitude of the carbon stock increases presented in this study are higher than those reported by previous estimates (Table 3). For example, Fang et al. [1] estimated the carbon sink of vegetation biomass in China at [+0.096, +0.106] Pg C year^{-1} between 1981 and 2000 using forest inventory data. Piao et al. [2] estimated the terrestrial carbon sink of China at +0.177 Pg C year^{-1} for the same period, of which 58% (+0.105 Pg C year^{-1}) was attributed to

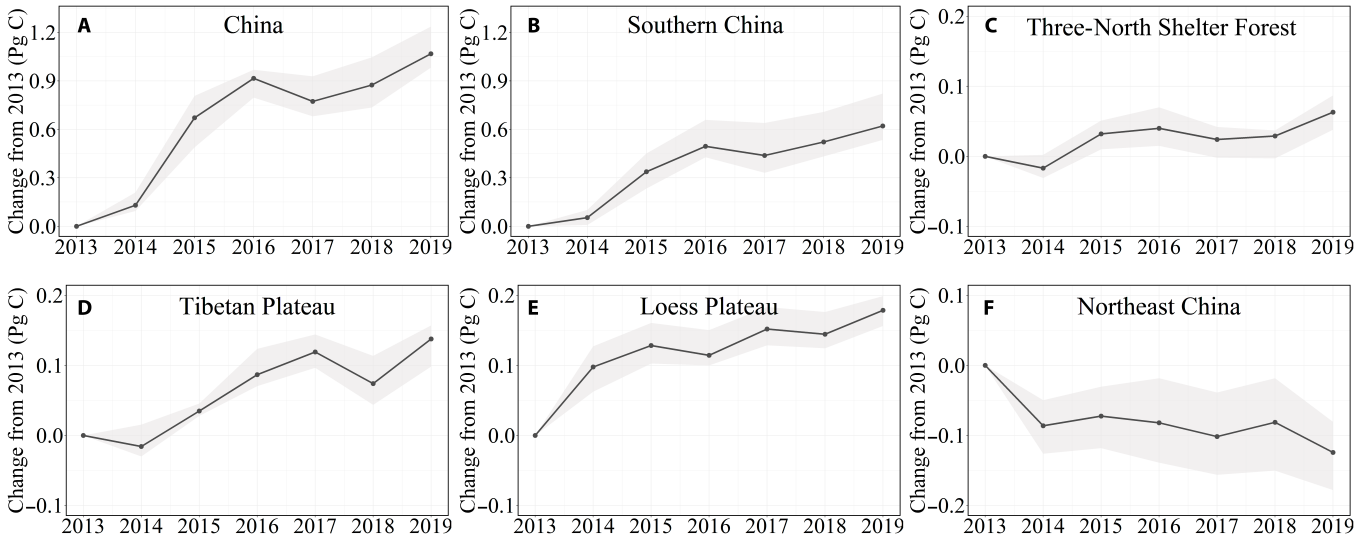

Fig. 9. Temporal variations in annual AGC (Pg C), expressed as the difference from 2013 values. (A) Annual variations in AGC in (A) China, (B) Southern China, (C) Three-North Shelter Forest, (D) Tibetan Plateau, (E) Loess Plateau, and (F) Northeast China.

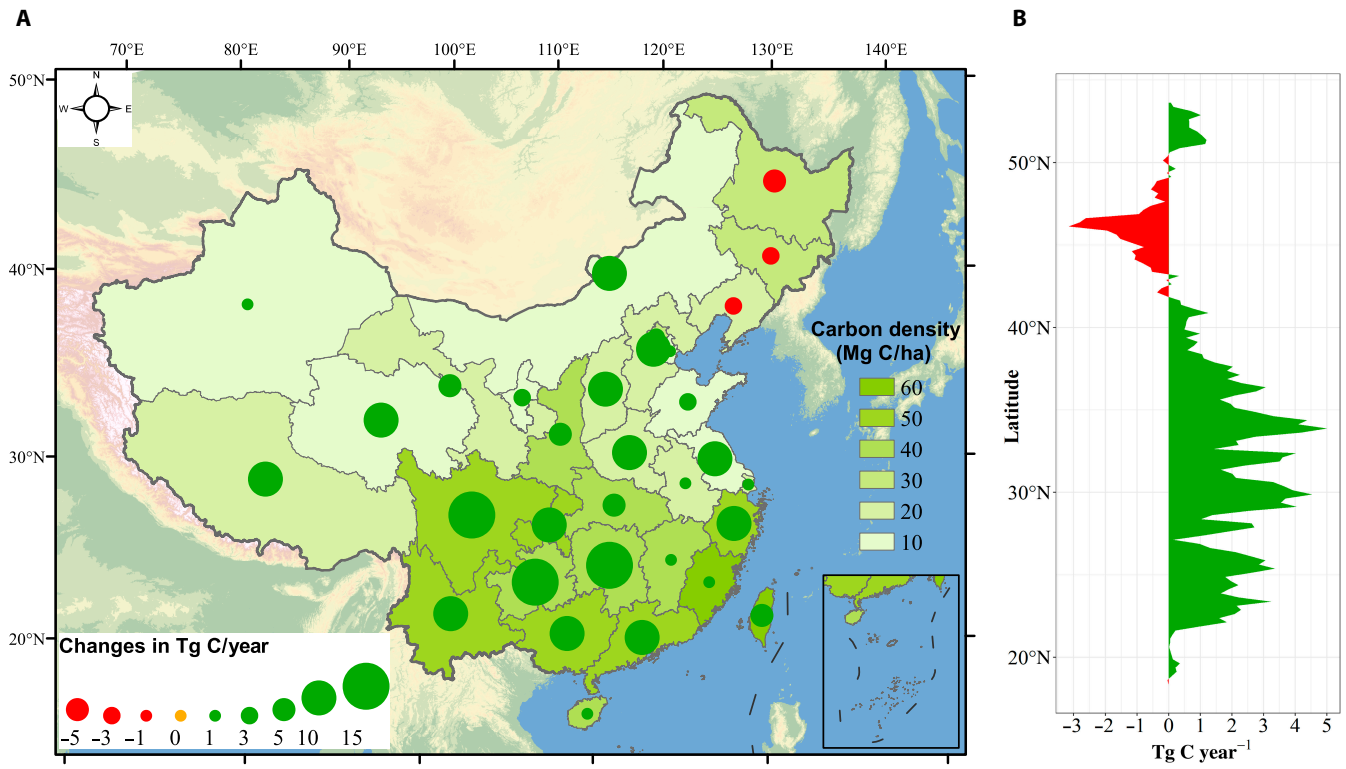

Fig. 10. Spatial patterns of the net AGC dynamics across China during 2013 to 2019. (A) Average AGC density (in Mg C/ha) and net AGC change for 2013 to 2019 summed for each province (in Tg C year^{-1}). (B) Net AGC change for 2013 to 2019 (summed per latitude). The corresponding pixel-scale AGC dynamics are shown in Fig. 11.

vegetation biomass. Our estimations of the biomass carbon stock increases are also higher than the estimates from Pan et al. [90], who reported a forest carbon sink of +0.12 Pg C year^{-1} in China during 2000 to 2007 using inventory data. This difference suggests that forest biomass carbon gains in the 2010s substantially increased in comparison to the 1980s and 1990s in China.

Limitations of this study

High uncertainties in our AGC estimates were observed in regions with low AGC density. This is the case also in other studies analyzing remote-sensing AGC retrievals. For example, AGC benchmark maps mainly derived from GLAS LiDAR observations have high uncertainties at low AGC density [7]. This could be explained by the fact that GLAS LiDAR shots only marked forest canopies as valid observations; thus, the regions with low AGC density (e.g., nonforest regions) could be inaccurately estimated [21]. However, considering the limited contribution of areas with low AGC density to the AGC dynamics over China, the impact of the low performance of AGC estimates at low AGC density is limited.

Table 3. Carbon sinks (Pg C year^{-1}) for China documented in the scientific literature.

Category	Carbon sink	Period	Method	Reference
Vegetation	0.096–0.106	1980s–1990s	Inventory	Fang et al. [1]
	0.105 ± 0.048	1980s–1990s	Inventory	Piao et al. [2]
	0.092 ± 0.074	1980s–1990s	Process model	Piao et al. [2]
	0.17 ± 0.06	2000s	Inventory	Jiang et al. [11]
	0.17	2013–2019	Maps	Xu et al. [21]
Forest	0.075 ± 0.035	1980s–1990s	Inventory	Fang et al. [1]
	0.13 ± 0.04	2000s	Inventory	Jiang et al. [11]
	0.104	2000s	Inventory	Jiang et al. [11]
	0.115	2000s	Inventory	Pan et al. [90]
	0.14	2000–2019	Maps	Harris et al. [87]
	0.17	2013–2019	VOD and VI	Our study

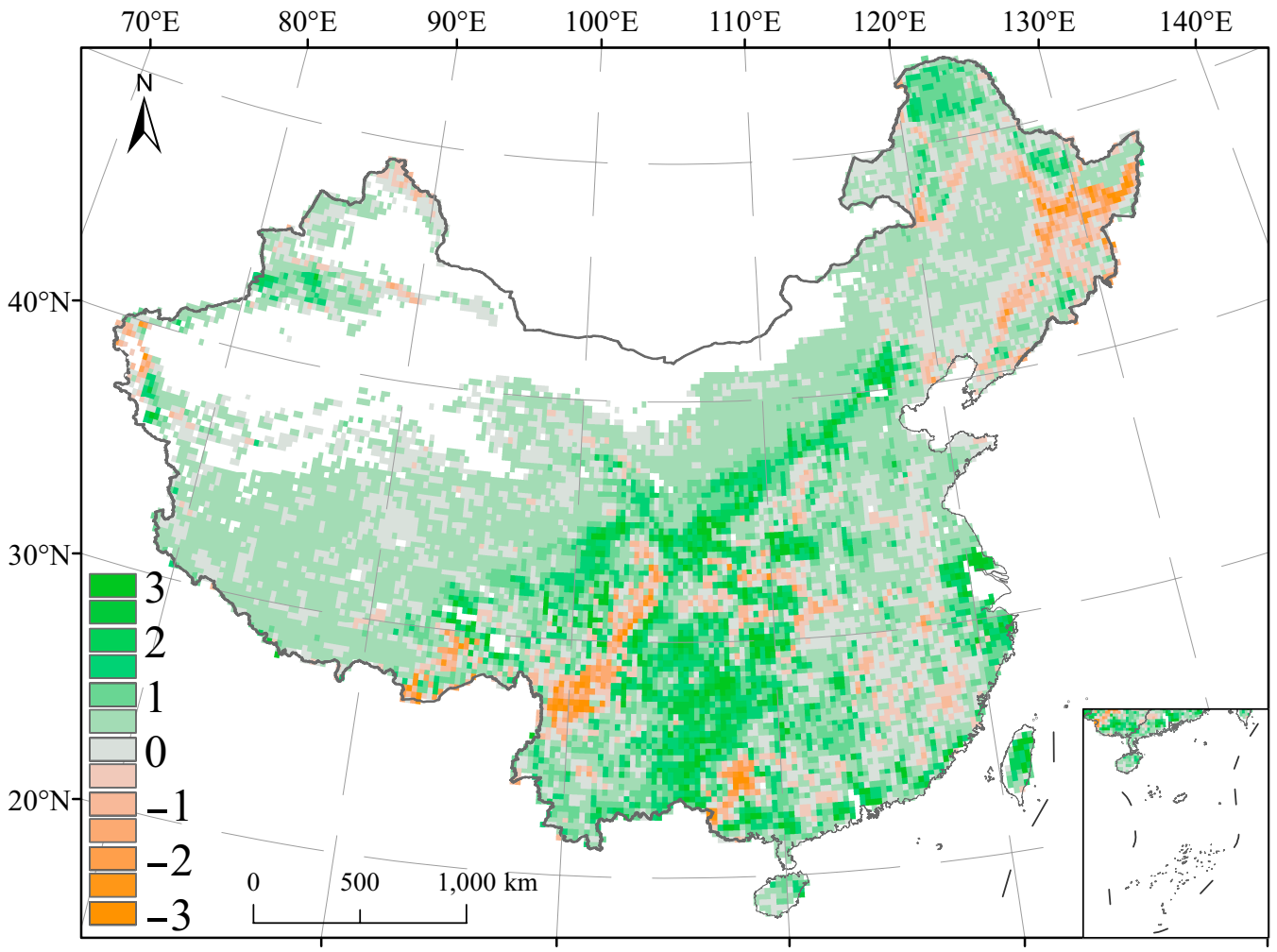

Fig. 11. Net AGC change in China during 2013 to 2019 (Mg C ha^{-1} $year^{-1}$). Note: Negative values are carbon sources.

To gap-fill the missing observations of L-VOD (Fig. S6), a merging model was proposed to produce a more spatially complete coverage of the China AGC product. Effects of RFI on L-VOD, which vary in both space and time, could affect our estimates of the interannual variations of AGC. Meanwhile, the effects of RFI on L-VOD leads to missing observations and limits its applicability for monitoring seasonal variation of AGC over some regions in China [6]. However, the RFI effects on L-VOD have strongly decreased over China since 2016 [47].

The coarse spatial resolution (0.25°) of our AGC product limits its applicability for monitoring fine-scale carbon losses and gains, e.g., related to disturbance regimes. As different land cover types are often mixed within a single pixel, the carbon change of AGC observed in a 0.25° grid cell comprises all land covers including forests and nonforest ecosystems, representing a mix of different processes (e.g., deforestation, forest degradation, and reforestation). Our pixel-level estimates of AGC sinks are admittedly conservative as a result of the coarse spatial resolution of the VOD product, which inevitably represents averaged estimates.

Considering the large spatial mismatch between AGC estimates (0.25°) and point-scale measurements, direct evaluation of the AGC estimates compared with in situ measurements will result in large bias, especially over strongly mixed 0.25° pixels, e.g., mixed pixels including dense and low-density forests. A bootstrapped cross-validation method was used here to evaluate the uncertainties associated with the AGC estimates, but further independent evaluations using local carbon density estimated by airborne LiDAR are needed to better evaluate the performance of our AGC model. It is also noteworthy that the uncertainties of the AGC estimates computed from different calibration models were inconsistent (Fig. 12). For example, the calibrated AGC models have different uncertainties based on the Saatchi (Fig. 12A) and CCI benchmark maps (Fig. 12B), where uncertainties larger than 100% covered 6.6% and 10.9% of China, respectively. The higher uncertainties (>100%) in our AGC estimates were mainly observed in northern China and the eastern Tibetan Plateau and may be related to topography in those mountainous regions. Areas of high uncertainties in the AGC estimates calibrated with the CCI map displayed a larger coverage than for the others benchmark maps. In the most southern and southwestern regions of China, the majority of the uncertainties of the AGC estimates are smaller than 10%.

Conclusions

This study provided the first comprehensive assessment of optical VIs and microwave VODs for monitoring spatial patterns of AGC in China, demonstrating the capabilities in the synergistic use of VODs and VIs to provide an explicit quantification

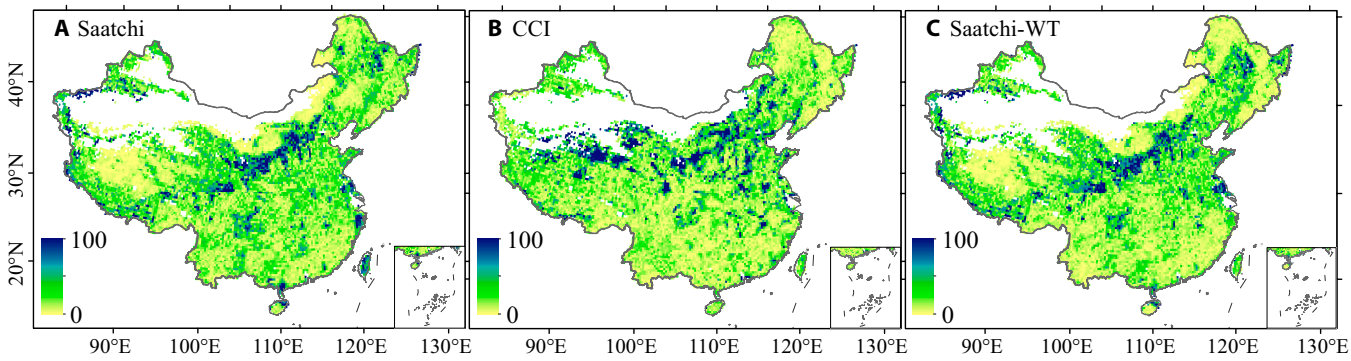

Fig. 12. Maps of the uncertainties associated with AGC_{merge} ($Uncertainties_{pixel}$) relative to different benchmark AGC maps in 2015. Maps of $Uncertainties_{pixel}$ relative to the benchmark AGC maps of (A) Saatchi, (B) CCI, and (C) Saatchi-WT.

of the AGC dynamics across large scales. It is worth noting that the validation for the estimated AGC product is not based on measured AGC, limited by the availability of in situ measurements at a large scale (e.g., larger than 0.25°). Thus, further independent evaluations using local carbon density estimated by airborne LiDAR or forest inventory data are needed to validate our results. Especially, with the recent and future launches of Chinese HJ-1C [94], Britain's NovaSAR-S [95], NASA's GEDI [29], ICESat-2 [96], NISAR [97], and ESA's BIOMASS [75,98], more biomass products will be good candidates for improving the accuracy of continental AGC maps following the approach presented in this study. In future, the carbon dynamics found by this study will be analyzed using ancillary data on climate changes and forest disturbances, to better understand and reveal the drivers of China carbon dynamics.

Acknowledgments

Funding: This work was supported by the National Science Fund for Distinguished Young Scholars (41825020), the National Natural Science Foundation of China (42171339), the Postdoctoral Start-Up Project of Southwest University (SWU020016), and the Strategic Priority Research Program of the Chinese Academy of Sciences (XDA05050200). **Author contributions**: L.F., J.-P.W., Y.-P.W., and J.Y. designed the experiment. Z.C. and L.F. conducted the analysis and wrote the manuscript. J.-P.W., Y.-P.W., P.C., J.Y., J.C., R.F., J.M.C., W.Y., W.J., Xin L., F.F., F.J., M.W., Y.Q., Xiaojun L., and X.T. revised the manuscript and provided valuable suggestions. All authors contributed to the discussion and revised the submitted manuscript. **Competing interests:** The authors declare that they have no competing interests.

Data Availability

The data that support the findings of this study are available at National Tibetan Plateau Data Center, DOI: 10.11888/Terre.tpdc.272887.

Supplementary Materials

Supplementary data associated with this article can be found in Supplementary Materials.
Supplementary Text.
Figs. S1 to S6.
Tables S1 and S2.

References

1. Fang J, Guo Z, Piao S, Chen A. Terrestrial vegetation carbon sinks in China, 1981–2000. *Sci China Ser D Earth Sci*. 2007;50(9):1341–1350.
2. Piao S, Fang J, Ciais P, Peylin P, Huang Y, Sitch S, Wang T. The carbon balance of terrestrial ecosystems in China. *Nature*. 2009;458(7241):1009–1013.
3. Fang J, Yu G, Liu L, Hu S, Chapin FS III. Climate change, human impacts, and carbon sequestration in China. *Proc Natl Acad Sci USA*. 2018;115(16):4015–4020.
4. He H, Wang S, Zhang L, Wang J, Ren X, Zhou L, Piao S, Yan H, Ju W, Gu F, et al. Altered trends in carbon uptake in China's terrestrial ecosystems under the enhanced summer monsoon and warming hiatus. *Natl Sci Rev*. 2019;6(3):505–514.
5. Baccini A, Goetz SJ, Walker WS, Laporte NT, Sun M, Sulla-Menashe D, Hackler J, Beck PSA, Dubayah R, Friedl MA, et al. Estimated carbon dioxide emissions from tropical deforestation improved by carbon-density maps. *Nat Clim Chang*. 2012;2(3):182–185.
6. Fan L, Wigneron JP, Ciais P, Chave J, Brandt M, Fensholt R, Saatchi SS, Bastos A, Al-Yaari A, Hufkens K, et al. Satellite-observed pantropical carbon dynamics. *Nat Plants*. 2019;5(9):944–951.
7. Saatchi SS, Harris NL, Brown S, Lefsky M, Mitchard ET, Salas W, Zutta BR, Buermann W, Lewis SL, Hagen S, et al. Benchmark map of forest carbon stocks in tropical regions across three continents. *Proc Natl Acad Sci USA*. 2011;108(24):9899–9904.
8. Santoro M, Cartus O, Carvalhais N, Rozendaal DMA, Avitabile V, Araza A, de Bruin S, Herold M, Quegan S, Rodríguez-Veiga P, et al. The global forest above-ground biomass pool for 2010 estimated from high-resolution satellite observations. *Earth Syst Sci Data*. 2021;13(8):3927–3950.
9. Su Y, Guo Q, Xue B, Hu T, Alvarez O, Tao S, Fang J. Spatial distribution of forest aboveground biomass in China: Estimation through combination of spaceborne lidar, optical imagery, and forest inventory data. *Remote Sens Environ*. 2016;173:187–199.
10. Wigneron J-P, Fan L, Ciais P, Bastos A, Brandt M, Chave J, Saatchi S, Baccini A, Fensholt R. Tropical forests did not recover from the strong 2015–2016 El Niño event. *Sci Adv*. 2020;6(6):Article eaay4603.
11. Jiang F, Chen JM, Zhou L, Ju W, Zhang H, Machida T, Ciais P, Peters W, Wang H, Chen B, et al. A comprehensive estimate

of recent carbon sinks in China using both top-down and bottom-up approaches. *Sci Rep*. 2016;6:Article 22130.
12. Wang J, Feng L, Palmer PI, Liu Y, Fang S, Bosch H, O'Dell CW, Tang X, Yang D, Liu L, et al. Large Chinese land carbon sink estimated from atmospheric carbon dioxide data. *Nature*. 2020;586(7831):720–723.
13. Myneni RB, Dong J, Tucker CJ, Kaufmann RK, Kauppi PE, Liski J, Zhou L, Alexeyev V, Hughes MK. A large carbon sink in the woody biomass of northern forests. *Proc Natl Acad Sci USA*. 2001;98(26):14784–14789.
14. Chen JM, Ju W, Ciais P, Viovy N, Liu R, Liu Y, Lu X. Vegetation structural change since 1981 significantly enhanced the terrestrial carbon sink. *Nat Commun*. 2019;10(1):Article 4259.
15. Avitabile V, Herold M, Heuvelink GB, Lewis SL, Phillips OL, Asner GP, Armston J, Ashton PS, Banin L, Bayol N, et al. An integrated pan-tropical biomass map using multiple reference datasets. *Glob Chang Biol*. 2016;22(4):1406–1420.
16. Blackard J, Finco M, Helmer E, Holden G, Hoppus M, Jacobs D, Lister A, Moisen G, Nelson M, Riemann R. Mapping U.S. forest biomass using nationwide forest inventory data and moderate resolution information. *Remote Sens Environ*. 2008;112(4):1658–1677.
17. Nelson R, Margolis H, Montesano P l, Sun GQ, Cook B, Corp L, Andersen H, deJong B, Pellat FP, Fickel T, et al. Lidar-based estimates of aboveground biomass in the continental US and Mexico using ground, airborne, and satellite observations. *Remote Sens Environ*. 2017;188:127–140.
18. Hu T, Su Y, Xue B, Liu J, Zhao X, Fang J, Guo Q. Mapping global forest aboveground biomass with spaceborne LiDAR, optical imagery, and forest inventory data. *Remote Sens*. 2016;8(7):565.
19. Huang H, Liu C, Wang X, Zhou X, Gong P. Integration of multi-resource remotely sensed data and allometric models for forest aboveground biomass estimation in China. *Remote Sens Environ*. 2019;221:225–234.
20. Zhang R, Zhou X, Ouyang Z, Avitabile V, Qi J, Chen J, Giannico V. Estimating aboveground biomass in subtropical forests of China by integrating multisource remote sensing and ground data. *Remote Sens Environ*. 2019;232:111341.
21. Xu L, Saatchi SS, Yang Y, Yu Y, Pongratz J, Bloom AA, Bowman K, Worden J, Liu J, Yin Y, et al. Changes in global terrestrial live biomass over the 21st century. *Sci Adv*. 2021;7(27):Article eabe9829.
22. Zhang Y, Liang S, Yang L. A review of regional and global gridded forest biomass datasets. *Remote Sens*. 2019;11(23):2744.
23. Baccini A, Walker W, Carvalho L, Farina M, Sulla-Menashe D, Houghton RA. Tropical forests are a net carbon source based on aboveground measurements of gain and loss. *Science*. 2017;358(6360):230–234.
24. Brandt M, Wigneron JP, Chave J, Tagesson T, Penuelas J, Ciais P, Rasmussen K, Tian F, Mbow C, Al-Yaari A, et al. Satellite passive microwaves reveal recent climate-induced carbon losses in African drylands. *Nat Ecol Evol*. 2018;2(5):827–835.
25. Tong X, Brandt M, Yue Y, Ciais P, Rudbeck Jepsen M, Penuelas J, Wigneron J-P, Xiao X, Song X-P, Horion S, et al. Forest management in southern China generates short term extensive carbon sequestration. *Nat Commun*. 2020;11(1):Article 129.
26. Liao Z, Van Dijk AIJM, He B, Larraondo PR, Scarth PF. Woody vegetation cover, height and biomass at 25-m resolution across Australia derived from multiple site, airborne and satellite observations. *Int J Appl Earth Obs Geoinf*. 2020;93:102209.
27. Myers-Smith IH, Kerby JT, Phoenix GK, Bjerke JW, Epstein HE, Assmann JJ, John C, Andreu-Hayles L, Angers-Blondin S, Beck PSA, et al. Complexity revealed in the greening of the Arctic. *Nat Clim Chang*. 2020;10(2):106–117.
28. Mitchard ET, Feldpausch TR, Brienen RJ, Lopez-Gonzalez G, Monteagudo A, Baker TR, Lewis SL, Lloyd J, Quesada CA, Gloor M, et al. Markedly divergent estimates of Amazon forest carbon density from ground plots and satellites. *Glob Ecol Biogeogr*. 2014;23(8):935–946.
29. Dubayah R, Blair JB, Goetz S, Fatoyinbo L, Hansen M, Healey S, Hofton M, Hurtt G, Kellner J, Luthcke S, et al. The Global Ecosystem Dynamics Investigation: High-resolution laser ranging of the Earth's forests and topography. *Sci Remote Sens*. 2020;1:Article 100002.
30. Jones MO, Kimball JS, Jones LA. Satellite microwave detection of boreal forest recovery from the extreme 2004 wildfires in Alaska and Canada. *Glob Chang Biol*. 2013;19(10):3111–3122.
31. Konings AG, Piles M, Rotzer K, McColl KA, Chan SK, Entekhabi D. Vegetation optical depth and scattering albedo retrieval using time series of dual-polarized L-band radiometer observations. *Remote Sens Environ*. 2016;172:178–189.
32. Liu YY, van Dijk AIJM, de Jeu RAM, Canadell JG, McCabe MF, Evans JP, Wang GJ. Recent reversal in loss of global terrestrial biomass. *Nat Clim Chang*. 2015;5(5):470–474.
33. Jackson TJ, Schmugge TJ. Vegetation effects on the microwave emission of soils. *Remote Sens Environ*. 1991;36(3):203–212.
34. Wigneron J-P, Kerr Y, Chanzy A, Jin Y-Q. Inversion of surface parameters from passive microwave measurements over a soybean field. *Remote Sens Environ*. 1993;46(1):61–72.
35. Du J, Kimball JS, Jones LA, Kim Y, Glassy J, Watts JD. A global satellite environmental data record derived from AMSR-E and AMSR2 microwave earth observations. *Earth Syst Sci Data*. 2017;9(2):791–808.
36. Liu X, Wigneron J-P, Fan L, Frappart F, Ciais P, Baghdadi N, Zribi M, Jagdhuber T, Li X, Wang M, et al. ASCAT IB: A radar-based vegetation optical depth retrieved from the ASCAT scatterometer satellite. *Remote Sens Environ*. 2021;264:112587.
37. Moesinger L, Dorigo W, de Jeu R, van der Schalie R, Scanlon T, Teubner I, Forkel M. The global long-term microwave vegetation optical depth climate archive (VODCA). *Earth Syst Sci Data*. 2020;12(1):177–196.
38. Tian F, Brandt M, Liu YY, Rasmussen K, Fensholt R. Mapping gains and losses in woody vegetation across global tropical drylands. *Glob Chang Biol*. 2017;23(4):1748–1760.
39. Wang M, Fan L, Frappart F, Ciais P, Sun R, Liu Y, Li X, Liu X, Moisy C, Wigneron J-P. An alternative AMSR2 vegetation optical depth for monitoring vegetation at large scales. *Remote Sens Environ*. 2021;263:112556.
40. Liu YY, de Jeu RAM, McCabe MF, Evans JP, van Dijk AIJM. Global long-term passive microwave satellite-based retrievals of vegetation optical depth. *Geophys Res Lett*. 2011;38(18):L18402.
41. Fernandez-Moran R, Al-Yaari A, Mialon A, Mahmoodi A, Al Bitar A, De Lannoy G, Rodriguez-Fernandez N, Lopez-Baeza E, Kerr Y, Wigneron J-P. SMOS-IC: An alternative SMOS soil moisture and vegetation optical depth product. *Remote Sens*. 2017;9(5):457.
42. Wigneron J-P, Jackson T, O'neill P, De Lannoy G, De Rosnay P, Walker J, Ferrazzoli P, Mironov V, Bircher S, Grant J. Modelling the passive microwave signature from land surfaces: A review of recent results and application to the L-band SMOS

& SMAP soil moisture retrieval algorithms. *Remote Sens Environ*. 2017;192:238–262.
43. Qin Y, Xiao X, Wigneron J-P, Ciais P, Brandt M, Fan L, Li X, Crowell S, Wu X, Doughty R, et al. Carbon loss from forest degradation exceeds that from deforestation in the Brazilian Amazon. *Nat Clim Chang*. 2021;11(5):442–448.
44. Konings AG, Piles M, Das N, Entekhabi D. L-band vegetation optical depth and effective scattering albedo estimation from SMAP. *Remote Sens Environ*. 2017;198:460–470.
45. Li B, Good SP, Urycki DR. The value of L-band soil moisture and vegetation optical depth estimates in the prediction of vegetation phenology. *Remote Sens*. 2021;13(7):1343.
46. Frappart F, Wigneron J-P, Li X, Liu X, Al-Yaari A, Fan L, Wang M, Moisy C, Le Masson E, Aoulad Lafkih Z, et al. Global monitoring of the vegetation dynamics from the vegetation optical depth (VOD): A review. *Remote Sens*. 2020;12(18):2915.
47. Wigneron J-P, Li X, Frappart F, Fan L, Al-Yaari A, De Lannoy G, Liu X, Wang M, Le Masson E, Moisy C. SMOS-IC data record of soil moisture and L-VOD: Historical development, applications and perspectives. *Remote Sens Environ*. 2021;254:112238.
48. Li X, Wigneron J-P, Frappart F, Fan L, Ciais P, Fensholt R, Entekhabi D, Brandt M, Konings AG, Liu X, et al. Global-scale assessment and inter-comparison of recently developed/reprocessed microwave satellite vegetation optical depth products. *Remote Sens Environ*. 2021;253:112208.
49. Mateo-Sanchis A, Piles M, Muñoz-Marí J, Adsuara JE, Pérez-Suay A, Camps-Valls G. Synergistic integration of optical and microwave satellite data for crop yield estimation. *Remote Sens Environ*. 2019;234:111460.
50. Prigent C, Jimenez C. An evaluation of the synergy of satellite passive microwave observations between 1.4 and 36 GHz, for vegetation characterization over the tropics. *Remote Sens Environ*. 2021;257:112346.
51. Tian F, Brandt M, Liu YY, Verger A, Tagesson T, Diouf AA, Rasmussen K, Mbow C, Wang YJ, Fensholt R. Remote sensing of vegetation dynamics in drylands: Evaluating vegetation optical depth (VOD) using AVHRR NDVI and *in situ* green biomass data over west African Sahel. *Remote Sens Environ*. 2016;177:265–276.
52. Grant JP, Wigneron JP, De Jeu RAM, Lawrence H, Mialon A, Richaume P, Al Bitar A, Drusch M, van Marle MJE, Kerr Y. Comparison of SMOS and AMSR-E vegetation optical depth to four MODIS-based vegetation indices. *Remote Sens Environ*. 2016;172:87–100.
53. Mialon A, Rodríguez-Fernández NJ, Santoro M, Saatchi S, Mermoz S, Bousquet E, Kerr YH. Evaluation of the sensitivity of SMOS L-VOD to Forest above-ground biomass at global scale. *Remote Sens*. 2020;12(9):1450.
54. Chaparro D, Duveiller G, Piles M, Cescatti A, Vall-llossera M, Camps A, Entekhabi D. Sensitivity of L-band vegetation optical depth to carbon stocks in tropical forests: A comparison to higher frequencies and optical indices. *Remote Sens Environ*. 2019;232:111303.
55. Rodríguez-Fernández NJ, Mialon A, Mermoz S, Bouvet A, Richaume P, Al Bitar A, Al-Yaari A, Brandt M, Kaminski T. An evaluation of SMOS L-band vegetation optical depth (L-VOD) data sets: High sensitivity of L-VOD to above-ground biomass in Africa. *Biogeosciences*. 2018;15(14):4627–4645.
56. Vittucci C, Vaglio Laurin G, Tramontana G, Ferrazzoli P, Guerriero L, Papale D. Vegetation optical depth at L-band and above ground biomass in the tropical range: Evaluating their relationships at continental and regional scales. *Int J Appl Earth Obs Geoinf*. 2019;77:151–161.
57. Gevaert AI, Parinussa RM, Renzullo LJ, van Dijk AIJM, de Jeu RAM. Spatio-temporal evaluation of resolution enhancement for passive microwave soil moisture and vegetation optical depth. *Int J Appl Earth Obs Geoinf*. 2016;45:235–244.
58. Schmidt L, Forkel M, Dorigo WA, Moesinger L, van der Schalie R, Yebra M, Pugh TA. Assessing the sensitivity of multi-frequency vegetation optical depth to biomass and canopy moisture content: Towards an ecological-oriented evaluation. *EGU General Assembly Conference Abstracts*; 2020. p. 10931.
59. Lawrence H, Wigneron J-P, Richaume P, Novello N, Grant J, Mialon A, Al Bitar A, Merlin O, Guyon D, Leroux D, et al. Comparison between SMOS vegetation optical depth products and MODIS vegetation indices over crop zones of the USA. *Remote Sens Environ*. 2014;140:396–406.
60. Potapov P, Li X, Hernandez-Serna A, Tyukavina A, Hansen MC, Kommareddy A, Pickens A, Turubanova S, Tang H, Silva CE, et al. Mapping global forest canopy height through integration of GEDI and Landsat data. *Remote Sens Environ*. 2021;253:112165.
61. Breiman L. Random forests. *Mach Learn*. 2001;45(1):5–32.
62. Zhang Y, Ma J, Liang S, Li X, Li M. An evaluation of eight machine learning regression algorithms for forest aboveground biomass estimation from multiple satellite data products. *Remote Sens*. 2020;12(24):4015.
63. Lu F, Hu H, Sun W, Zhu J, Liu G, Zhou W, Zhang Q, Shi P, Liu X, Wu X, et al. Effects of national ecological restoration projects on carbon sequestration in China from 2001 to 2010. *Proc Natl Acad Sci USA*. 2018;115(16):4039–4044.
64. Wigneron J-P, Kerr Y, Waldteufel P, Saleh K, Escorihuela MJ, Richaume P, Ferrazzoli P, de Rosnay P, Gurney R, Calvet JC, et al. L-band microwave emission of the biosphere (L-MEB) model: Description and calibration against experimental data sets over crop fields. *Remote Sens Environ*. 2007;107(4):639–655.
65. Hersbach H, Bell B, Berrisford P, Hirahara S, Horányi A, Muñoz-Sabater J, Nicolas J, Peubey C, Radu R, Schepers D, et al. The ERA5 global reanalysis. *Q J R Meteorol Soc*. 2020;146(730):1999–2049.
66. Kim Y, Kimball JS, Glassy J, Du J. An extended global Earth system data record on daily landscape freeze–thaw status determined from satellite passive microwave remote sensing. *Earth Syst Sci Data*. 2017;9(1):133–147.
67. Abbas S, Wong MS, Wu J, Shahzad N, Muhammad Irteza S. Approaches of satellite remote sensing for the assessment of above-ground biomass across tropical forests: Pan-tropical to National Scales. *Remote Sens*. 2020;12(20):3351.
68. Didan K. *MOD13A3 MODIS/Terra vegetation indices monthly L3 global 1km sin grid v006*. NASA EOSDIS Land Processes Distributed Active Archive Center; 2015.
69. Hmimina G, Dufrene E, Pontailler JY, Delpierre N, Aubinet M, Caquet B, de Grandcourt A, Burban B, Flechard C, Granier A, et al. Evaluation of the potential of MODIS satellite data to predict vegetation phenology in different biomes: An investigation using ground-based NDVI measurements. *Remote Sens Environ*. 2013;132:145–158.
70. Huete A, Didan K, Miura T, Rodriguez EP, Gao X, Ferreira LG. Overview of the radiometric and biophysical performance of the MODIS vegetation indices. *Remote Sens Environ*. 2002;83(1–2):195–213.

71. Myneni R, Knyazikhin Y, Park T. *MOD15A2H MODIS/terra leaf area index/FPAR 8-day L4 global 500 m SIN grid V006*. NASA EOSDIS Land Processes Distributed Active Archive Center; 2015.
72. Chen JM, Black T. Defining leaf area index for non-flat leaves. *Plant Cell Environ*. 1992;15(4):421–429.
73. Dimiceli C, Carroll M, Sohlberg R, Kim D, Kelly M, Townshend J. *MOD44B MODIS/Terra vegetation continuous fields yearly L3 global 250 m SIN grid V006*. NASA EOSDIS Land Processes Distributed Active Archive Center; 2015.
74. Hansen M, DeFries R, Townshend J, Carroll M, Dimiceli C, Sohlberg R. Global percent tree cover at a spatial resolution of 500 meters: First results of the MODIS vegetation continuous fields algorithm. *Earth Interact*. 2003;7(10):1–15.
75. Carreiras JMB, Quegan S, Le Toan T, Minh DHT, Saatchi SS, Carvalhais N, Reichstein M, Scipal K. Coverage of high biomass forests by the ESA BIOMASS mission under defense restrictions. *Remote Sens Environ*. 2017;196:154–162.
76. Santoro M, Cartus O. *ESA Biomass Climate Change Initiative (Biomass_CCI): Global datasets of forest above-ground biomass for the year 2017, v1*. Centre for Environmental Data Analysis; 2019.
77. Chang Z, Hobeichi S, Wang Y-P, Tang X, Abramowitz G, Chen Y, Cao N, Yu M, Huang H, Zhou G, et al. New Forest aboveground biomass maps of China integrating multiple datasets. *Remote Sens*. 2021;13(15):2892.
78. Liu J, Kuang W, Zhang Z, Xu X, Qin Y, Ning J, Zhou W, Zhang S, Li R, Yan C, et al. Spatiotemporal characteristics, patterns, and causes of land-use changes in China since the late 1980s. *J Geogr Sci*. 2014;24(2):195–210.
79. Tang X, Zhao X, Bai Y, Tang Z, Wang W, Zhao Y, Wan H, Xie Z, Shi X, Wu B, et al. Carbon pools in China's terrestrial ecosystems: New estimates based on an intensive field survey. *Proc Natl Acad Sci USA*. 2018;115(16):4021–4026.
80. Defourny P, Vancutsem C, Bicheron P, Brockmann C, Nino F, Schouten L, Leroy M. GLOBCOVER: a 300 m global land cover product for 2005 using Envisat MERIS time series. Paper presented at: Proceedings of ISPRS Commission VII Mid-Term Symposium: Remote Sensing: From Pixels to Processes; 2006 May 8; Enschede, Netherlands.
81. Entekhabi D, Reichle HR, Koster DR, Crow TW. Performance metrics for soil moisture retrievals and application requirements. *J Hydrometeorol*. 2010;11(3):832–840.
82. Sexton JO, Song X-P, Feng M, Noojipady P, Anand A, Huang C, Kim D-H, Collins KM, Channan S, DiMiceli C, et al. Global, 30-m resolution continuous fields of tree cover: Landsat-based rescaling of MODIS vegetation continuous fields with lidar-based estimates of error. *Int J Digit Earth*. 2013;6(5):427–448.
83. Song X, Huang C, Sexton JO, Feng M, Narasimhan R, Channan S, Townshend JR. An assessment of global forest cover maps using regional higher-resolution reference data sets. Paper presented at: 2011 IEEE International Geoscience and Remote Sensing Symposium; 2011 Jul 24–29; Vancouver, Canada.
84. Qin Y, Xiao X, Dong J, Zhou Y, Wang J, Doughty RB, Chen Y, Zou Z, Moore B III. Annual dynamics of forest areas in South America during 2007–2010 at 50-m spatial resolution. *Remote Sens Environ*. 2017;201:73–87.
85. Brandt M, Hiernaux P, Tagesson T, Verger A, Rasmussen K, Diouf AA, Mbow C, Mougin E, Fensholt R. Woody plant cover estimation in drylands from earth observation based seasonal metrics. *Remote Sens Environ*. 2016;172:28–38.
86. Li X, Al-Yaari A, Schwank M, Fan L, Frappart F, Swenson J, Wigneron JP. Compared performances of SMOS-IC soil moisture and vegetation optical depth retrievals based on tau-omega and two-stream microwave emission models. *Remote Sens Environ*. 2020;236:111502.
87. Harris NL, Gibbs DA, Baccini A, Birdsey RA, de Bruin S, Farina M, Fatoyinbo L, Hansen MC, Herold M, Houghton RA, et al. Global maps of twenty-first century forest carbon fluxes. *Nat Clim Chang*. 2021;11(3):234–240.
88. Brandt M, Yue Y, Wigneron JP, Tong X, Tian F, Jepsen MR, Xiao X, Verger A, Mialon A, al-Yaari A, et al. Satellite-observed major greening and biomass increase in South China karst during recent decade. *Earth's Future*. 2018;6:1017–1028.
89. Tong X, Brandt M, Yue Y, Horion S, Wang K, Keersmaecker WD, Tian F, Schurgers G, Xiao X, Luo Y, et al. Increased vegetation growth and carbon stock in China karst via ecological engineering. *Nat Sustain*. 2018;1(1):44–50.
90. Pan YD, Birdsey RA, Fang JY, Houghton R, Kauppi PE, Kurz WA, Phillips OL, Shvidenko A, Lewis SL, Canadell JG, et al. A large and persistent carbon sink in the World's forests. *Science*. 2011;333(6045):988–993.
91. Byrne B, Liu J, Lee M, Baker I, Bowman KW, Deutscher NM, Feist DG, Griffith DWT, Iraci LT, Kiel M, et al. Improved constraints on northern extratropical CO_2 fluxes obtained by combining surface-based and space-based atmospheric CO_2 measurements. *J Geophys Res Atmos*. 2020;125(15):Article e2019JD032029.
92. Jiang F, Wang H, Chen JM, Ju W, Tian X, Feng S, Li G, Chen Z, Zhang S, Lu X, et al. Regional CO_2 fluxes from 2010 to 2015 inferred from GOSAT XCO_2 retrievals using a new version of the global carbon assimilation system. *Atmos Chem Phys*. 2021;21(3):1963–1985.
93. Scholze M, Kaminski T, Knorr W, Voßbeck M, Wu M, Ferrazzoli P, Kerr Y, Mialon A, Richaume P, Rodríguez-Fernández N, et al. Mean European carbon sink over 2010–2015 estimated by simultaneous assimilation of atmospheric CO_2, soil moisture, and vegetation optical depth. *Geophys Res Lett*. 2019;46(23):13796–13803.
94. Du J, Shi J, Sun R. The development of HJ SAR soil moisture retrieval algorithm. *Int J Remote Sens*. 2010;31(14):3691–3705.
95. Bird R, Whittaker P, Stern B, Angli N, Cohen M, Guida R. NovaSAR-S: A low cost approach to SAR applications. Paper presented at: Conference Proceedings of 2013 Asia-Pacific Conference on Synthetic Aperture Radar (APSAR); 2013 Sep 23–27; Tsukuba, Japan.
96. Abdalati W, Zwally HJ, Bindschadler R, Csatho B, Farrell SL, Fricker HA, Harding D, Kwok R, Lefsky M, Markus T, et al. The ICESat-2 laser altimetry Mission. *Proc IEEE*. 2010;98(5):735–751.
97. Rosen PA, Hensley S, Shaffer S, Veilleux L, Chakraborty M, Misra T, Bhan R, Sagi VR, Satish R. The NASA-ISRO SAR mission - An international space partnership for science and societal benefit. Paper presented at: 2015 IEEE Radar Conference (RadarCon); 2015 May 10–15; Arlington, VA.
98. Quegan S, Toan LT, Chave J, Dall J, Exbrayat JF, Minh DHT, Lomas M, D'Alessandro MM, Paillou P, Papathanassiou K, et al. The European Space Agency BIOMASS mission: Measuring forest above-ground biomass from space. *Remote Sens Environ*. 2019;227:44–60.